Arctic stratocumulus in large-eddy simulations and a mixed-layer model

Xiyue Zhang[1], **Tapio Schneider**[1], **and Colleen M. Kaul** [1]

[1]Environmental Science and Engineering, California Institute of Technology, Pasadena, California, USA.

Key Points:

- Sensitivities of the Arctic stratocumulus to temperature, inversion strength, and humidity are explored through LES
- Mixed-layer theory explains most of the sensitivities, with minor discrepancies resulting from microphysical effects
- Sensitivity of the positive longwave cloud radiative feedback depends on the vertical structure of warming

Corresponding author: X. Zhang, xiyue@caltech.edu

Abstract

The stable and cloudy Arctic boundary layer (BL) is an essential component of the Arctic climate system and is often thought to contribute to Arctic amplification of global warming. However, regional and global climate models that depend on parameterized representations of BL turbulence and clouds show large spreads in simulated Arctic cloudiness. We use large-eddy simulations (LES) that explicitly resolve BL turbulence and clouds to explore the sensitivities of Arctic BL clouds to idealized climate change. Condensed water path is found to increase with BL temperature and free-tropospheric relative humidity, but it decreases with inversion strength across the BL top. The condensed water changes are indicative of a positive longwave cloud feedback as the Arctic warms, especially near the surface. The magnitude of the cloud feedback sensitivity depends the vertical structure of warming. The trends shown by the LES climate change experiments can be largely reproduced by a mixed-layer model that excludes microphysical processes. Thus, these results offer encouragement that analysis methods used to explain the sensitivities of lower-latitude BL clouds to climate change can be usefully extended to Arctic BL clouds.

1 Introduction

The Arctic boundary layer (BL) is known for its ubiquitous temperature inversion and the prevalent mixed-phase low clouds [*Curry et al.*, 1996]. Though the inversion strength and height vary from season to season, the overall inversion probability is as high as 90% [*Tjernström and Graversen*, 2009]. Many of these inversions are elevated, capping a well-mixed layer below. Annual-mean cloud fraction is around 70%, with a maximum greater than 80% in autumn [*Wang and Key*, 2005; *Kay and L'Ecuyer*, 2013]. These characteristics have manifold impacts on high-latitude climate. For example, Arctic clouds warm the surface in all seasons but summer because their longwave greenhouse effect predominates over shortwave effects, unlike for their subtropical counterparts [*Intrieri et al.*, 2002; *Kay and L'Ecuyer*, 2013]. Therefore, Arctic cloud feedbacks may operate differently from those at lower latitudes. Moreover, anomalous spring-time clouds have been postulated to influence the autumn sea ice minimum through long-term effects on the surface energy balance [*Cox et al.*, 2016].

Climate change in the polar regions has interested scientists since the first modeling studies of the effects of increased CO_2 concentrations. Climate models robustly show Arctic amplification under greenhouse warming [*Manabe and Wetherald*, 1975; *Holland and Bitz*, 2003]. In the recent decades, the Arctic indeed has been experiencing rapid changes. The Arctic sea ice extent, most prominently in September, has shrunk substantially since the beginning of the modern satellite record [*Stroeve et al.*, 2012]. Amplified warming in high northern latitudes has also been observed over the past decades, especially in winter [*Schneider and Held*, 2001; *Cohen et al.*, 2014]. This warming has been observed to be surface intensified [*Screen et al.*, 2012], with trends that can be discerned in observational records despite the large internal variability in high latitudes [*Serreze et al.*, 2009]. Furthermore, significant increases in specific humidity have been observed, but relative humidity changes are more complex [*Sherwood et al.*, 2010; *Serreze et al.*, 2012]. Cloud feedbacks and the trapping of heat under the stable inversion are thought to contribute to Arctic amplification of global warming [*Wetherald and Manabe*, 1975; *Holland and Bitz*, 2003; *Graversen and Wang*, 2009; *Pithan and Mauritsen*, 2014]. However, the sign of any cloud feedback in high latitudes is uncertain [*Kay et al.*, 2016]. In GCMs, low clouds depends on parameterizations for turbulence and convection, which are developed mainly for lower latitudes. In fact, GCMs show large spread in the simulated seasonal cycle of Arctic cloud fraction [*Vavrus et al.*, 2009; *Karlsson and Svensson*, 2013]. A key step towards constraining Arctic cloud feedbacks is to identify robust mechanisms of how the clouds respond to changes in temperature, inversion strength, and moisture content of the free troposphere.

Recent modeling studies have focused on microphysical and dynamical processes maintaining Arctic mixed-phase stratocumulus clouds. *Savre et al.* [2015] investigated how the persistence of Arctic mixed-phase clouds depends on microphysical processes and moisture sources in the sub-cloud layer and in the free troposphere. They found that microphysical processes (ice sublimation) play an important role in controlling the BL structure. A more idealized study by *Solomon et al.* [2014] found a similar role for ice microphysics in controlling BL moisture. One important question that was not addressed by either study is how Arctic mixed-phase clouds respond to climate change. How will the low cloud properties change as the Arctic warms?

Here we use large-eddy simulations (LES) with the recently developed Python Cloud Large Eddy Simulation code (PyCLES) [*Pressel et al.*, 2015] to investigate systematically the response of Arctic BL clouds to different kinds of idealized changes. We base our study on the Indirect and Semi-direct Aerosol Campaign (ISDAC) LES intercomparison study [*Ovchinnikov et al.*, 2014]. In an idealized setup (hereafter ISDAC-i) mimicking conditions during the ISDAC observational campaign, we investigate the sensitivities of Arctic mixed-phase stratocumulus clouds to temperature, cloud-top inversion strength, and free-tropospheric moisture. These are important factors controlling stratocumulus properties [*Dal Gesso et al.*, 2014; *van der Dussen et al.*, 2015], and understanding them is a first step toward understanding how Arctic low clouds respond to climate change. We then use a mixed-layer model (MLM) to elucidate the cloud response to perturbations seen in the LES. MLMs have been extensively used to study stratocumulus-

topped BLs over subtropical oceans [*Lilly*, 1968; *Bretherton and Wyant*, 1997; *Dal Gesso et al.*, 2014; *De Roode et al.*, 2014], but rarely Arctic BL clouds. Yet they turn out to be similarly useful for providing insight into controls of Arctic stratocumulus clouds.

We begin by describing the LES and MLM used in the study. Then we specify the experimental setup of the original ISDAC LES intercomparison and ISDAC-i. We justify the ISDAC-i setup by characteristics of the projected Arctic warming. Next we show the results from ISDAC and ISDAC-i simulations, followed by discussion.

2 Model Descriptions

2.1 LES Code

We work with the recently developed PyCLES code, which uses total water specific humidity and specific entropy as prognostic variables to solve the anelastic equations of motion [*Pressel et al.*, 2015]. PyCLES has been used successfully to simulate subtropical marine BL clouds [*Tan et al.*, 2016, 2017; *Pressel et al.*, 2017]. This is its first application in a polar setting.

We use a nominally 5th-order Weighted Essentially Non-Oscillatory (WENO5) advection scheme for momentum and scalars, and a strong stability preserving 3rd-order, 3-stage Runge-Kutta method for time-stepping. The time-steps are adaptive with a target Courant number of 0.7. The numerical dissipation implicit in the WENO scheme is used in lieu of an explicit subgrid-scale dissipation scheme, as this has been found to lead to the most faithful simulation of subtropical stratocumulus [*Pressel et al.*, 2017]. We only use a Smagorinsky-Lilly subgrid-scale closure near the surface to transfer momentum between the LES domain and the surface. Monin-Obukhov similarity theory is used to compute the surface flux of momentum at the lower boundary. The roughness length is set to 4×10^{-4} m. The surface sensible and latent heat fluxes are zero for all simulations presented in this study. The grid resolution is 50 m in the horizontal, with doubly periodic boundary conditions, and 10 m in the vertical. The computational domain extends 3.2 km $\times$ 3.2 km in the horizontal and is 2.56 km deep in the vertical.

2.1.1 Microphysics

The modeling of mixed-phase microphysics remains an active area of research. We use a relatively simple one-moment microphysics scheme that captures basic features of Arctic mixed-phase clouds [*Kaul et al.*, 2015]. Cloud condensates are diagnosed using an empirical partition function $f(T)$ that models the liquid fraction λ of the condensate as a function of temperature [*Grabowski*, 1998; *Kaul et al.*, 2015; *Pressel et al.*, 2015],

$$\lambda(T) = \begin{cases} 0 & \text{for } T < T_i, \\ \left(\dfrac{T - T_i}{T_f - T_i}\right)^n & \text{for } T_i \le T \le T_f, \\ 1 & \text{for } T_f < T, \end{cases} \tag{1}$$

where $T_f = 273.15$ K is the freezing point, $T_i \approx 235$ K is the homogeneous nucleation temperature. The exponent n here is chosen to be 0.1 [*Kaul et al.*, 2015], justified by the fact that liquid fractions close to 80% at 240–250 K have been observed in Arctic low clouds [*de Boer et al.*, 2009].

The same partition function (1) is used to determine the effective specific latent heat L in the mixed phase and a thermodynamically consistent saturation vapor pressure [*Pressel et al.*, 2015]. Precipitation species (rain and snow) are prognostic. The processes that govern the transformation between species include autoconversion, aggregation, and phase changes. Sedimentation of cloud condensate is not taken into account. The scheme uses exponential particle size distribution functions for rain, ice, and snow. Cloud ice has a constant intercept parameter $N_{0,\text{ice}} =$

1×10^7 m^{-4}. The snow intercept parameter $N_{0,\mathrm{snow}}$ is a diagnostic function of snow specific humidity [*Morrison et al.*, 2011]. More details of the scheme are given in *Kaul et al.* [2015].

We made several minor modifications to the microphysical source terms in *Kaul et al.* [2015]. The thermodynamic variable G, which represents the vapor diffusion of an ice-water sphere and determines the mass growth rate of liquid droplets or ice crystals, is taken without approximation, following *Straka* [2009], as

$$G(T,P) = \left[\frac{\rho_{l/i} R_v T}{D p_v^*(T)} + \left(\frac{L}{R_v T} - 1\right)\frac{L\rho_{l/i}}{\kappa T}\right]^{-1}.$$

Here, $\rho_{l/i}$ is the density of liquid or ice, depending on the process, L is the effective latent heat, and p_v^* is the saturation vapor pressure; D is the water vapor diffusivity, which increases with temperature and decreases with pressure; and κ is the thermal conductivity, which depends approximately linearly on temperature. The detailed formulations of D and κ are given in *Straka* [2009]. The function G increases approximately exponentially with temperature and is used in formation (autoconversion), evaporation, and deposition/sublimation of droplets and ice crystals.

The formation of precipitation and evaporation/sublimation of hydrometeors contribute to the entropy tendency. The small heat transfer and the aerodynamic drag during sedimentation are also included in the entropy source/sink terms, as specified in *Pressel et al.* [2015].

2.1.2 Radiative Transfer

The default ISDAC longwave radiation scheme is idealized and depends solely on cloud liquid water content [*Ovchinnikov et al.*, 2014]. In order to capture radiative flux changes under climate change, we use the RRTMG [*Iacono et al.*, 2008] integrated into PyCLES. Additional information on temperature, humidity, and ozone above the LES domain is required to calculate radiative fluxes. Therefore, the standard atmospheric profiles from the Mixed-Phase Arctic Cloud Experiment (M-PACE) LES intercomparision project are patched to the ISDAC temperature and humidity profiles. RRTMG produces a more realistic radiative flux profile, which results in slightly warmer BL compared to the ISDAC simulations with idealized radiation. RRTMG is called every 60 simulated seconds in PyCLES.

The liquid effective radius entering the radiative transfer calculation uses the parameterization by *Martin et al.* [1994] for warm stratocumulus clouds [*Blossey et al.*, 2013; *Tan et al.*, 2016]. The mean ice effective radius follows an empirical relation that depends on temperature and ice water content [*Boudala et al.*, 2002],

$$r_{e,\mathrm{ice}} = 34.419\ \mu\mathrm{m} \times \left(\frac{\mathrm{IWC}}{1\ \mathrm{g\ m^{-3}}}\right)^{0.06} \exp\left[0.013\ \mathrm{K^{-1}}(T - 273.15\ \mathrm{K})\right],$$

where IWC is the ice water concentration (units of g m^{-3}). The mean ice effective radius is mainly a function of temperature and increases with temperature at a rate of $\sim 0.5\ \mu\mathrm{m\ K^{-1}}$. It is only sensitive to IWC at low IWC values [*Boudala et al.*, 2002]. Only cloud ice is included in the radiative transfer calculation. The ice effect on cloud infrared optical depth is minimal because the cloud layer is dominated by the optically thick liquid water.

2.2 Mixed-layer Model

We use a MLM with liquid-ice potential temperature θ_{li}, total water specific humidity q_t, and BL height z_i as prognostic variables [*Lilly*, 1968; *Bretherton and Wyant*, 1997; *Dal Gesso*

et al., 2014]:

$$\frac{dz_i}{dt} = w_e + w_{LS}(z_i), \tag{2}$$

$$\frac{d\theta_{li}}{dt} = \frac{1}{z_i}\left(w_e \Delta\theta_{li} - \frac{\Delta F_R}{\rho_a c_p}\right), \tag{3}$$

$$\frac{dq_t}{dt} = \frac{1}{z_i} w_e \Delta q_t. \tag{4}$$

Here, w_e is the cloud-top entrainment rate, w_{LS} is the large-scale subsidence rate as a function of height, and ρ_a is the mean density of air. The Δ variables represent contrasts across the entire BL. For example, $\Delta F_R = F_R^+ - F_{R,0}$ represents the total radiative flux contrast between the fluxes at the BL top and at the surface (see Table **??** for a list of variables). The same phase partitioning (1) is used to diagnose cloud liquid and ice water specific humidity q_l and q_i. Microphysical processes are not included in the MLM. A standard saturation adjustment procedure is called to get q_l and q_i at every time step, which then go into radiative transfer calculations. Time-stepping uses a 2nd-order 2-stage Runge-Kutta method with fixed time steps of 300 s. Radiative transfer uses the same RRTMG scheme as PyCLES and is called at every time step. Only the longwave radiative flux profile from RRTMG is used to calculate the radiative fluxes in (3). After the BL values are obtained at each time step, vertical profiles are calculated using the prescribed free tropospheric conditions as upper boundary conditions. The MLM vertical resolution is 5 m.

An entrainment rate formula is needed to close the set of MLM equations. Because of the lack of surface heat fluxes, turbulence in the BL is mostly driven by cloud-top radiative cooling. We parameterize the entrainment rate as

$$w_e = \underbrace{a\frac{\Delta_i F_R}{\rho_a c_p \Delta\theta_{li}}}_{\text{direct}} + \underbrace{w_0}_{\text{indirect}}, \tag{5}$$

where a = 0.85 and w_0 = 0.0004 m s^{-1} are constants diagnosed from ISDAC-i LES simulations. This is in line with assuming a direct and an indirect contribution of radiation to the mean entrainment rate [*Mellado*, 2017]. We define Δ_i to be the jump across the entrainment zone, more specifically the difference in values between the top of the well-mixed layer and the level at which turbulence goes to zero. For the prognostic variables, Δ_i and Δ are equivalent. BL height z_i, predicted by the MLM, lies within the entrainment zone. We assume that $\Delta\theta_{li} \approx \Delta_i\theta_v$ and that the longwave radiative flux jumps nearly discontinuously by $\Delta_i F_R$ at the cloud tops, driving radiative cooling at the top and with it the mixed-layer turbulence. Note that $\Delta_i F_R$ is usually less than the total radiative flux contrast ΔF_R [*Moeng*, 2000]. The direct term in (5) arises in an integration of the buoyancy budget across the BL top [*Moeng et al.*, 1999; *Stevens*, 2006]. Details of the entrainment parameterizations are described in Appendix A: .

3 Experimental Setup

3.1 ISDAC LES Intercomparison

The ISDAC LES intercomparison is based on observations of a long-lived mixed-phase stratocumulus cloud on April 26-27, 2008 north of Barrow, Alaska [*Ovchinnikov et al.*, 2014]. Soundings at Barrow show a stable surface layer below a well-mixed cloud layer. The boundary layer is capped by a strong potential temperature inversion, with a dry free atmosphere above.

Our setup generally follows the ISDAC LES intercomparison (see the Appendix A of *Ovchinnikov et al.* [2014]). We define θ_{li} following *Tripoli and Cotton* [1981] and *Pressel et al.* [2015] as

$$\theta_{li} = \theta \exp\left(-\frac{L}{T c_p}\frac{q_l + q_i}{1 - q_t}\right), \tag{6}$$

where the effective specific latent heat L is a weighted sum of that for vaporization and sublimation, using the partition function (1) as weight. Surface heat fluxes are set to zero because the fluxes over sea ice were negligible during the field campaign [*Ovchinnikov et al.*, 2014]. Large-scale subsidence is specified to be linear with height below the initial inversion at 825 m altitude, and it is constant with height above:

$$w_{LS} = \begin{cases} -5 \times 10^{-6}\ \mathrm{s}^{-1} \cdot z, & z < 825\ \mathrm{m}, \\ -4.125 \times 10^{-3}\ \mathrm{m\ s}^{-1}, & z \geq 825\ \mathrm{m}. \end{cases} \tag{7}$$

This choice of subsidence profile is justified in *Ovchinnikov et al.* [2014], and it is kept fixed for all simulations here. In addition to the large-scale subsidence, relaxation of the prognostic variables above 1200 m altitude toward the initial conditions is also included. Relaxation is specified as an additional source term in the prognostic equations. We relax specific entropy s (a native PyCLES variable instead of the otherwise common liquid-ice potential temperature) and total water specific humidity q_t toward the initial profiles above 1200 m, with a relaxation timescale of 1 hour. Horizontal velocities are relaxed toward the initial profiles throughout the domain with a timescale of 2 hours. The simulation is run for 8 hour integration time.

3.2 ISDAC-i: Idealized Climate Change

The initially decoupled surface layer does not persist and becomes well-mixed in the ISDAC simulations (Figure 2). Therefore, we initialize ISDAC-i with well-mixed profiles of θ_{li} and q_t below the inversion at height z_i. This allows the free troposphere to be the only source of moisture for the cloud (apart from recycling of moisture), and it shortens the equilibration time of the simulations. The initial profiles are (Figure 1):

$$\theta_{li} = \begin{cases} \theta_{li,0}, & z \leq z_i \\ \theta_{li,0} + \Delta\theta_{li} + \Gamma_\theta (z - z_i), & z > z_i \end{cases}$$

$$q_t = \begin{cases} q_{t,0}, & z \leq z_i, \\ q_s(T)\mathcal{H}_f, & z > z_i. \end{cases}$$

Here, $q_{t,0} = q_s(T_0)\mathcal{H}_0$, where q_s is the saturation specific humidity, T_0 is the surface temperature, and $\mathcal{H}_0 = 0.8$ is a near-surface relative humidity. This setup allows q_t to respond to temperature changes for a fixed relative humidity. We assume potential temperature lapse rate Γ_θ and relative humidity $\mathcal{H}_f$ that are constant with height above the cloud top (see Table **??** for default values). This setup enables us to explore different initial conditions that help us to gain insight into climate change in polar regions.

Idealized climate change studies are conducted by varying three variables (Table 1):

1. *Initial mixed-layer liquid-ice potential temperature* $\theta_{li,0}$. Changing only $\theta_{li,0}$ produces uniform warming or cooling in the entire domain. We vary $\theta_{li,0}$ from 4 K cooler to 8 K warmer, while the highest temperature at the surface is close to the freezing temperature. Beyond this temperature, we can no longer justify negligible surface heat fluxes when the surface is ice-free.
2. *Inversion strength* $\Delta\theta_{li}$. Temperature inversions are a common feature in and above the Arctic BL. The frequency of occurrence is as high as 90%, with a typical strength of 5–10 K [*Tjernström and Graversen*, 2009]. Changing $\Delta\theta_{li}$ can be thought of as changing the horizontal advection in the free troposphere from lower latitudes, or as changing the degree to which warming is surface amplified. We expect the inversion to weaken in a warmer climate, as the warming is surface amplified [*Screen et al.*, 2012]. The inversion strength directly affects entrainment processes at the cloud top and the amount of free-tropospheric moisture. We would like to distinguish the inversion strength from the commonly used lower-tropospheric stability (LTS), generally defined as the potential temperature difference between at 700 hPa and the surface [*Klein and Hartmann*,

1993]. LTS cannot distinguish surface inversions from the elevated inversions that occur in all seasons in the Arctic, and it does not directly determine the cloud-top entrainment process. Thus, the inversion strength on which we focus is more directly relevant for BL processes.

3. *Relative humidity in the free troposphere* $\mathcal{H}_f$. Typical values of relative humidity in the lower free troposphere at 70N are about 60% to 70%. The projected relative humidity change with warming in climate models is negligible in this region [*Sherwood et al.*, 2010]. Therefore, we run a set of simulations with $\mathcal{H}_f = 60\%$, then compare them to those with $\mathcal{H}_f = 70\%$. We fix the value of $\mathcal{H}_f$ and determine $\Delta q_t = q_s(T^+)\mathcal{H}_f - q_{t,0}$ from temperature and relative humidity across the cloud top. Although Δq_t is the relevant variable for cloud-top entrainment, prescribing Δq_t can lead to unreasonable relative humidity $\mathcal{H}_f$,which in reality is controlled by the large-scale circulation. For example, if we fix Δq_t instead of $\mathcal{H}_f$ while changing $\theta_{li,0}$ and $\Delta\theta_{li}$, $\mathcal{H}_f$ varies from 40 to 80%.

We ran 32 simulations with different initial conditions, each for 24 hours. Due to the setup of ISDAC-i, there is no surface heat flux to balance the cloud-top entrainment. Most simulations cannot reach a steady state over the simulated time we consider here. Therefore, we analyze both the end states and the time tendencies of the BL sensitivities.

4 Results

4.1 Comparison with LES Intercomparison

Figure 2 shows the domain-mean profiles of liquid-ice potential temperature θ_{li}, total-water specific humiditiy q_t, liquid-water specific humidity q_l, and the sum of ice and snow specific humidity $q_i + q_{\text{snow}}$, all averaged over the last hour of the simulation. Observations gathered by the National Research Council of Canada Convair-580 aircraft from ISDAC flight 31 are also shown for comparison [*McFarquhar et al.*, 2011]. Data are binned at a vertical interval of 50 m for the in-cloud measurements of temperature, humidity, and liquid and ice water contents. Also shown are the mean and 15–85 percentile range of the ISDAC LES model intercomparison [*Ovchinnikov et al.*, 2014]. As in the simulations in the ISDAC LES intercomparison study, the BL in our simulation becomes well mixed as turbulence generated by cloud-top radiative cooling mixes the cloud and sub-cloud layer. The initially stable layer near the surface is not maintained in our simulations; cloud-top radiative cooling leads to a BL that is cooler than was observed. A mixed-phase cloud layer of $\sim$300 m thickness persists throughout the simulation (Figure 3). Although the initial liquid water specific humidity q_l is within the observed range, it becomes greater than observed at the end of the simulation. This is consistent with the cooler θ_{li} profile, allowing more condensation than the initial conditions. The ISDAC intercomparison setup lacks large-scale forcing, which could keep the BL from cooling and deviating away from the initial conditions. The resulting biases can reinforce themselves through cloud-top radiative cooling, until radiation and subsidence warming become comparable.

The observed total ice water specific humidity, which includes cloud ice and snow (observations do not distinguish cloud ice from snow), shows large variance (Figure 2d). Our LES overestimates q_i at the cloud top, but it underestimates the snow below. The shape of our ice profile arises because q_i is diagnosed and takes the same shape as q_l, while q_{snow} is prognostic and has a peak at cloud base. Liquid water path (LWP) at the end of the eighth hour in our simulation is 39 g m^{-2}, which is within the range of the intercomparison values (Figure 3). The sum of ice water path (IWP) and snow water path (SWP) is 4 g m^{-2}, also within the range of the intercomparison [*Ovchinnikov et al.*, 2014]. Using data from the ISDAC flight 31, we estimate the LWP to be 3.7–24 g m^{-2}, and IWP to be 3.1–11 g m^{-2}. Other studies have estimated different values, for example, *Fan et al.* [2011] suggest LWP and IWP to be of comparable magnitudes of 5–8 g m^{-2}. *Savre et al.* [2014] use LWP of 8–16 g m^{-2} and IWP of 4–10 g m^{-2} as the observational references for their benchmark simulation. One should also

be aware of the uncertainties associated with the aircraft observations. *Fan et al.* [2011] implies that the measured ice water content's uncertainty is up to 100%. Nevertheless, both PyCLES and the LES intercomparison tend to overestimate LWP and produce IWP at the lower end of the observations.

Models with more complex bulk microphysics schemes still tend to underestimate q_i and IWP [*Ovchinnikov et al.*, 2014]. However, LES with bin microphysics schemes produce higher IWP, and so do bulk schemes whose particle slope distribution is fitted to resemble that of the bin schemes. Unfortunately, such ice properties cannot be derived from observations so far [*Fridlind and Ackerman*, 2018]. We recognize the underproduction of ice compared to observations, and focus our study on the macrophysical dynamics. Given our relatively simple treatment of microphysics, our LES captures the main features of the BL during ISDAC as well as other LES in the intercomparison.

To check for convergence of the simulations, we ran the ISDAC case with increased domain size and reduced horizontal grid spacing. Doubling the domain size and/or the horizontal resolution (halving the grid spacing) produced no significant changes to the results (not shown, in agreement with *Kaul et al.*, 2015).

4.2 ISDAC-i

4.2.1 LES

We first show the domain mean profiles at the 24th hour (Figure 4) and timeseries (Figure 5) of three selected cases to demonstrate the different simulations. In addition to the *baseline* simulation that is close to the ISDAC intercomparison ($\theta_{li,0} = 265$ K, $\Delta\theta_{li} = 5$ K), we also choose to present a *warm* case ($\theta_{li,0} = 273$ K, $\Delta\theta_{li} = 3$ K), and a *cold* case ($\theta_{li,0} = 261$ K, $\Delta\theta_{li} = 9$ K). We choose these three cases as examples because warming in the Arctic is surface intensified, and we can interpret it as a combined effect of uniform warming and a weakened elevated inversion. Therefore, we use the term "surface intensified warming" to refer to increasing $\theta_{li,0}$ together with decreasing $\Delta\theta_{li}$. On the other hand, "uniform warming" refers to changing only $\theta_{li,0}$. All three cases consist of well-mixed BLs with light snow. The most significant feature in the θ_{li} and q_t profiles is the increase of inversion height z_i from *cold* to *warm* (Figure 4a and b), which corresponds to an increase of cloud thickness z_c (Figure 5a).

Cloud liquid q_l increases with Arctic warming (Figure 4c, Figure 5b), yet the cloud ice shows a non-monotonic response (Figure 4d, Figure 5c). The amount of ice depends on the liquid fraction λ and total cloud condensate, which both vary with temperature. Given a fixed total cloud condensate amount, ice water decreases with Arctic warming because λ increases with temperature. Although the total cloud condensate still increases under uniform warming in ISDAC-i, λ increases more rapidly, leading to a lowered ice water amount under surface intensified warming. But snow, unlike cloud ice, is a prognostic variable. Its amount depends on microphysical processes. Autoconversion is the dominant source term for snow, and it increases significantly under surface intensified warming. SWP increases monotonically with Arctic warming, similarly to LWP (Figure 5d). There is no significant rain in the ISDAC-i simulations.

To further emphasize that the BLs are indeed well-mixed in ISDAC-i, Figure 6 shows the profiles of vertical velocity variance $\overline{w'w'}$ and vertical flux of virtual potential temperature $\overline{w'\theta'_v}$ (approximating the buoyancy production of TKE) for the three cases. A single peak in $\overline{w'w'}$ is found for each case, as is common in well-mixed BLs. The shape of the $\overline{w'\theta'_v}$ profile is the result of a combination of cloud processes [*Stull*, 1988]. The negative peak at the cloud top is indicative of entrainment, and the positive peak in the cloud is the evidence of longwave radiative cooling. The flux vanishes at the surface due to the absence of surface heating. The positive $\overline{w'\theta'_v}$ below the cloud layer confirm the lack of decoupling in all three cases. This means that microphysical processes in ISDAC-i are too weak to cause decoupling, which

is observed in other Arctic cases [*Solomon et al.*, 2014]. The significant increase of turbulent fluxes with surface intensified warming is mainly driven by stronger cloud radiative cooling due to higher q_l. Figure 7 shows the clear sky and cloudy radiative heating rates. Note that the clear sky values are an order of magnitude smaller than the radiative heating rates due to clouds. The cloudy radiative heating rate maximum nearly doubles as we move from the *cold* to the *warm* case.

When we increase the relative humidity above the inversion $\mathcal{H}_f$ from 60% to 70%, similar sensitivities to Arctic warming are seen (dashed lines in Figure 4 to 7). Free-tropospheric specific humidity increases accordingly, reducing the entrainment drying at the cloud top. In the *cold* case, a weak moisture inversion, a frequently observed feature in the Arctic BL [*Curry et al.*, 1996; *Sedlar and Tjernström*, 2009], is present (Figure 4b). Turbulence is slightly weakened in the *baseline* and the *warm* cases (Figure 6), despite an increase in LWP with $\mathcal{H}_f$ (Figure 5). One may expect that higher LWP is associated with stronger cloud-top radiative cooling, which drives increased turbulent mixing. This is indeed the case when $\mathcal{H}_f$ is fixed while the other two parameters are varied. However, when we only increase $\mathcal{H}_f$, LWP increases, and increased condensate weakens the turbulence (citation?).

Having looked at the individual cases, next we present domain mean quantities averaged for the last hour of each simulation. We display the results in a gridded parameter space spanned by inversion strength (x-axis) and uniform temperature change (y-axis). We first focus on cases with $\mathcal{H}_f = 60\%$. Figure 8 (top panels) show the LWP, IWP, and SWP of 16 simulations with $\mathcal{H}_f = 60\%$. LWP is sensitive to both the inversion strength and temperature: it decreases as the cloud-top inversion strengthens, and increases as the atmosphere warms uniformly. IWP, on the other hand, shows an opposite sensitivity to uniform warming. This is because with uniform warming, the ice fraction $1 - \lambda$ decreases strongly, notwithstanding that the total water path increases. Therefore, IWP decreases with uniform warming. In general, the amount of cloud ice is an order of magnitude less than cloud liquid, and it has negligible radiative effects on the BL. SWP responds mainly to inversion strength; it decreases as the inversion strengthens.

Another relevant quantity is the BL height z_i, here defined as the cloud top height (the first level from the top down that has non-zero q_l or q_i). As shown in Figure 9, z_i is mostly a function of inversion strength. The main processes that determine z_i are cloud-top entrainment and large-scale subsidence, as made explicit in the mass balance (2) of the MLM. In the MLM framework, w_e is inversely proportional to the inversion strength, as suggested by (5). Large-scale subsidence is fixed for all cases. We thus expect z_i to decrease monotonically with inversion strength, as long as $\Delta_i F_R$ does not increase to compensate. Cloud base height z_b shows a similar sensitivity to z_i. Both z_i and z_b increases slightly with uniform warming. However, cloud thickness ($z_c = z_i - z_b$) decreases with uniform warming. This suggests parameters in addition to w_e influence the sensitivity of z_b to uniform warming. We will discuss this further in the MLM section.

Next we examine theoretically how LWP varies with temperature and inversion strength. The nearly adiabatic liquid layers in the ISDAC-i LES simulations allow us to approximate LWP as

$$\mathrm{LWP} \simeq \frac{1}{2}\rho_a z_c^2 \Gamma_l, \tag{8}$$

where Γ_l is the liquid water lapse rate. Hence, we can further decompose the fractional changes in LWP into contributions from fractional changes in z_c and Γ_l:

$$\frac{\delta \mathrm{LWP}}{\mathrm{LWP}} \approx \frac{\delta \Gamma_l}{\Gamma_l} + 2\frac{\delta z_c}{z_c} \tag{9}$$

Figure 10 shows the decomposition of LWP fractional changes referenced to the *baseline* simulation. LWP increases diagonally towards warmer and weaker inversion cases, resembling Figure 8 for the LES qualitatively. The increase of LWP with temperature is due to increased Γ_l,

as can be seen from the expression for Γ_l in the absence of precipitation,

$$\Gamma_l \equiv \frac{dq_l}{dz} = -\frac{dq_s(T)}{dz}. \tag{10}$$

For a saturated cloud layer, the moist static energy is conserved if hydrostaticity is assumed. Therefore,

$$c_p dT + g dz + L_v dq_s = 0,$$

which we can rearrange to get

$$\frac{dq_s}{dz} = -\frac{c_p}{L_v}\left(\frac{g}{cp} + \frac{dT}{dz}\right). \tag{11}$$

By combining (10) and (11), we have an analytical expression for Γ_l:

$$\Gamma_l = \frac{c_p}{L_v}\left(\Gamma_d - \Gamma_m\right). \tag{12}$$

Figure 11 shows the fractional change of Γ_l with respect to temperature at 900 hPa. Because Γ_l is higher at warmer temperature, $(1/\Gamma_l)(d\Gamma_l/dT)$ decreases with temperature. The second term on the right hand side of (9) changes similarly to the cloud thickness (compare the third panels in Figures 9 and 10). Both $\delta\Gamma_l/\Gamma_l$ and $2\delta z_c/z_c$ are of comparable magnitudes given the parameter variations in ISDAC-i.

When $\mathcal{H}_f$ is increased from 60% to 70%, the patterns of the main BL variables discussed above remain unchanged (compare bottom panels to top panels in Figures 8, 9, and 10). The most significant changes are the magnitudes of LWP and z_i. This is evident in Figure 10, where $2\delta z_c/z_c$ in the *warm* case becomes more dominant as $\mathcal{H}_f$ increases. Cloud base height z_b is insensitive to $\mathcal{H}_f$, thus the increase in z_c is due to higher z_i (Figure 9). In fact, the entrainment rate increases slightly with $\mathcal{H}_f$. One might expect that a drier free troposphere promotes stronger entrainment via the cloud top entrainment instability (CTEI) mechanism [*Deardorff*, 1980; *Wood*, 2012]. We do not observe such mechanism in our ISDAC-i simulations. All of the simulations without specific humidity inversion at the cloud top satisfy neither the original nor the modified CTEI criteria [*Wood*, 2012]. Here w_e increases with $\mathcal{H}_f$ because more moisture is entrained from the cloud top to form liquid water, which increases the cloud-top radiative cooling rate and hence entrainment.

The use of a full radiative transfer model allows us to infer cloud radiative feedbacks from ISDAC-i simulations by looking at the top-of-atmosphere (TOA) cloud radiative effect ($\mathrm{CRE_{LW}}$). It is defined as the difference between the all-sky and clear-sky TOA net longwave fluxes. Negative $\mathrm{CRE_{LW}}$ means the presence of clouds allows less longwave radiation to leave the top of the atmosphere. As shown in Figure 12, $\mathrm{CRE_{LW}}$ increases weakly with uniform warming, but much more prominently with a stronger temperature inversion. As the Arctic warms, $\mathrm{CRE_{LW}}$ decreases, implying a positive LW cloud feedback at TOA. From *cold* to *baseline*, a near-surface temperature increase of 4 K is associated with 1.5 W $\mathrm{m^{-2}}$ decrease of $\mathrm{CRE_{LW}}$. From *baseline* to *warm*, the near surface temperature increase is 8 K, doubling that from *cold* to *baseline*, but $\mathrm{CRE_{LW}}$ only decreases by 1.8 W $\mathrm{m^{-2}}$. The estimated sensitivities are 0.37 and 0.23 W $\mathrm{m^{-2}}$ $\mathrm{K^{-1}}$ accordingly. If we look at the entire parameter range, the weakest sensitivity is associated with warming uniformly without changing the inversion strength. On the other hand, the strongest sensitivity involves minor uniform warming but significantly weaker inversions. The values vary from 0.015 to 0.85 W $\mathrm{m^{-2}}$ $\mathrm{K^{-1}}$, suggesting an important role the vertical structure of warming plays in high-latitude LW cloud feedbacks. By contrast, for a 10% increase in $\mathcal{H}_f$, changes in $\mathrm{CRE_{LW}}$ are negligible.

4.2.2 MLM

The same set of ISDAC-i simulations are run using the MLM. We will again analyze the results in the parameter space of inversion strength and temperature. Figures 13 to 15 are

to be compared with Figures 8 to 10. Figure 16 compares the magnitudes of LWP, z_i and inversion properties in the two models. The most significant difference is in LWP, where the MLM produces a pattern with curved rather than linear contours (Figure 13). Most of the LWP gradients occur at cases with stronger inversions. LWP decreases with inversion strength and is insensitive to temperature change for cases with stronger inversion ($\Delta\theta_{li} \geq 7$ K). The minimal LWP occurs at $\Delta\theta_{li} = 9$ K, $\theta_{li,0} = 273$ K, whereas for LES it occurs at at $\Delta\theta_{li} = 9$ K, $\theta_{li,0} = 261$ K.

The magnitude of LWP is significantly higher in MLM, especially for cases with $\mathcal{H}_f = 70\%$ (Figure 16a). The difference between MLM and LES LWP due to $\mathcal{H}_f$ changes is nearly constant across cases, shown by the distance to the 1:1 line on Figure 16a. IWP is higher in the MLM than in LES, but how it varies with inversion strength and uniform temperature changes is very similar in the two models.

The higher condensate amount in MLM can be attributed to thicker cloud layers (Figure 14 and Figure 16b). On average, clouds are 50 m thicker in MLM than in LES. When the inversion is weak, cloud thickness is insensitive to uniform temperature changes in LES (z_i and z_b change at the same rate). This is not the case in MLM, due of a lack of direct response of entrainment to uniform temperature changes (see Eq. (5)). There is also a bias in z_b, mostly due to a mismatch in q_t. Because precipitation is weak in the ISDAC-i simulations, cloud-top entrainment is the main process that determines q_t.

In MLM, everything above z_i is prescribed and does not vary with time. In LES, processes such as radiation and subsidence can change the profiles of θ_{li} and q_t above the cloud top up to 1200 m. Above 1200 m, θ_{li} and q_t are nudged toward the initial profiles. The lapse rate right above the cloud top is smoothed due to radiative cooling, especially for cases with a strong inversion. Therefore, $\Delta\theta_{li}$ in MLM is slightly biased high compared to LES (Figure 16c). This explains the difference in entrainment rates between the models. Furthermore, right above z_i, subsidence dries the air and creates a vertically uniform q_t profile (instead of q_t decreasing with height in LES), making Δq_t in MLM biased high (Figure 16d). This leads to a positive bias in MLM q_t values, which makes z_b lower than in LES.

In order to understand how cloud thickness changes, it is necessary to know what governs the changes of cloud base height z_b. We can derive the rate of change of z_b in the MLM framework. Start by defining

$$z_b = \frac{1}{\Gamma_d}\left(T_0 - T_{\mathrm{LCL}}\right),$$

where Γ_d is the dry adiabatic lapse rate, and T_{LCL} is the temperature at the lifting condensation level, which is assumed to coincide with z_b. To compare the rate of change of z_b to the mass balance (2), we differentiate

$$\frac{dz_b}{dt} = \frac{1}{\Gamma_d}\left(\frac{dT_0}{dt} - \frac{dT_{\mathrm{LCL}}}{dt}\right). \tag{13}$$

The rate of change of surface temperature T_0 is implied by the energy balance (3). The temperature at z_b is T_{LCL}, defined as

$$q_t = q_s(T_{\mathrm{LCL}}).$$

We can take the time derivative and use the chain rule to get the time rate of change of T_{LCL},

$$\frac{dT_{\mathrm{LCL}}}{dt} = \frac{dq_t}{dt}\beta, \tag{14}$$

where

$$\beta = \left(\frac{dq_s}{dT}\Big|_{T_{\mathrm{LCL}}}\right)^{-1}.$$

By plugging (14) into (13) and using (3), (4), and (5), we find

$$\frac{dz_b}{dt} = \frac{1}{\Gamma_d z_i \rho_a c_p}\left[a\Delta_i F_R\left(1 - \beta\frac{\Delta q_t}{\Delta\theta_{li}}\right) - \Delta F_R\right]. \tag{15}$$

Cloud base height, unlike cloud top height, not only depends on entrainment rate, but also on temperature (through β), the total radiative flux contrast across the BL, and the specific humidity jump Δq_t.

Cloud base height z_b is controlled by several factors, and we focus on their relative importance. The first term in the squared bracket on the right hand side of (15) involves mostly entrainment processes such as contrasts of radiative fluxes, q_t, and θ_{li} across the cloud top. Embedded in the first term is the dependence on temperature through β, where β decreases with temperature. However, both Δq_t and $\Delta\theta_{li}$ increase strongly with inversion strength, which overcomes the temperature dependence of β. Consequently, the first term dominates z_b changes in the parameter ranges of ISDAC-i.

5 Discussion and Conclusions

To improve our understanding of the sensitivity of Arctic low clouds to climate change, we simulated a mixed-phase stratocumulus using the recently developed LES code PyCLES. The setup was based on the ISDAC LES intercomparison project, and the simulated BL agrees reasonably well with aircraft observations. Subsequently, we conducted sensitivity experiments in a modified ISDAC setup.

By varying parameters that control the initial BL structure, such as temperature, inversion strength, and free-tropospheric relative humidity, we explored the BL response to different climates in an idealized setting (termed ISDAC-i experiments). We showed that Arctic stratocumulus can be represented well with a MLM, as long as the BL does not become strongly decoupled. Most cases studied here have a cloud layer dominated by liquid, with amounts close to be adiabatic, despite an increase of sub-adiabaticity in cases with high free-tropospheric relative humidity.

The adiabatic LWP increases with $\theta_{li,0}$ and $\mathcal{H}_f$, and it decreases with $\Delta\theta_{li}$. This can be understood in the MLM framework through the dependence of the liquid water lapse rate and cloud thickness on the three parameters. Most of the LES have similar parameter dependencies as those exposed by the MLM, despite differences in the magnitude of the LWP sensitivities. The LWP response suggests a positive longwave cloud feedback at TOA, as the Arctic moves toward a warmer state that is surface intensified so the inversion weakens. The sensitivity depends on the structure of warming, which varies from 0.015 to 0.85 W m^{-2} K^{-1}. Cloud ice amounts are an order of magnitude smaller than liquid amounts, and ice has a small radiative effect on TOA budgets.

The ability of the MLM to reproduce LES results depends on the fact that the BL remains coupled in our ISDAC-i simulations. Microphysical processes have the potential to decouple the BL by transporting moisture from the cloud layer downward. Sublimation of snow in the sub-cloud layer may cool the air, thus leading to decoupling. In our simulations, microphysics alone were unable to decouple the BL in ISDAC-i. External forcing such as large-scale advection appears to be needed to maintain a decoupled surface layer [*Savre et al.*, 2015].

The three parameters we chose to vary have implications for Arctic climate change. For example, surface amplified warming is likely to reduce the inversion strength capping the BL. When this occurs over sea ice, where surface fluxes are weak, we expect LWP to increase based on our experiments. A positive longwave cloud feedback results. If a decrease of free-tropospheric relative humidity accompanies warming in the Arctic, it would imply a change in LWP sensitivity to inversion strength and uniform warming (Figure 13).

Our study of the sensitivity of Arctic stratocumulus is largely inspired by the subtropical marine stratocumulus literature [*Dal Gesso et al.*, 2014; *van der Dussen et al.*, 2015]. The cloud thinning with uniform warming that we found in ISDAC-i is consistent with studies of subtropical stratocumulus. However, the LWP in subtropical stratocumulus decreases with uniform warming and cloud thinning, which is opposite to what we see in ISDAC-i. This is due

to the fact that in ISDAC-i, q_l remains close to adiabatic and its response to warming overcomes the cloud thinning. As shown in Figure 11, we expect the fractional change of liquid water lapse rate to decrease in warmer temperatures. This seems to explain the weaker liquid water lapse rate effect in the subtropics. Also, our temperature perturbation is much larger than the 2-K perturbation that is used in most subtropical studies. The longwave cloud radiative effect we find from ISDAC-i is weak but positive. The strength of this LW cloud feedback also depends on inversion strength, and hence on the vertical structure of warming. Two features distinguish our study from the subtropical ones. First, surface heat fluxes are set to zero, so the surface fluxes do not respond to perturbations. Second, decoupling of the BL does not occur in the parameter ranges we explored.

The simplified ISDAC-i setup has its limitations. For example, we have not tested the sensitivities of the BL and clouds to surface fluxes. As sea ice extent continues to decline in the Arctic Ocean, surface heat fluxes will become more important in driving BL turbulence. A closed surface energy budget is needed to explore radiative feedbacks in a consistent manner. A next step is to investigate how such surface flux changes and other changes in the large-scale circulation can affect Arctic low-cloud cover more broadly.

Table 1. List of parameters and ranges over which they are varied in the sensitivity studies with ISDAC-i. Baseline parameter values in bold.

Variable	Range
$\theta_{li,0}$	261, **265**, 269, 273 K
$\Delta\theta_l i$	3, **5**, 7, 9 K
$\mathcal{H}_f$	**60**, 70%

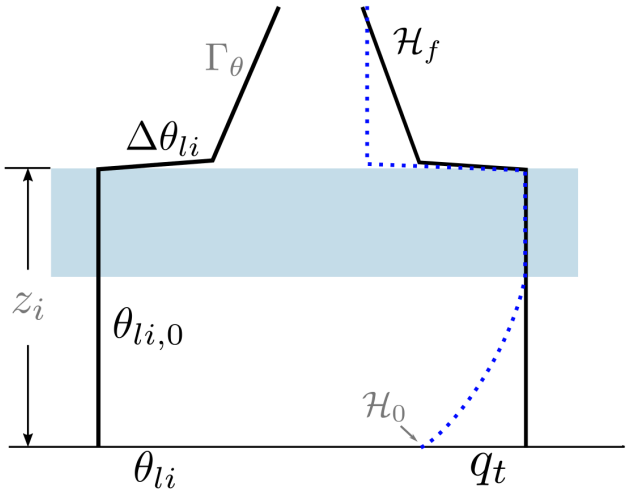

Figure 1. Schematic of the ISDAC-i θ_{li} and q_t initial conditions. The cloud layer is indicated in blue. The BL with height z_i has constant θ_{li} and q_t, where q_t is determined by the relative humidity (blue dotted line) near the surface $\mathcal{H}_0$. The BL is capped by an inversion of $\Delta\theta_{li}$, above which potential temperature increases with height at the rate Γ_θ. Relative humidity above the BL ,$\mathcal{H}_f$, does not vary with height, and it is used to determine q_t above z_i.

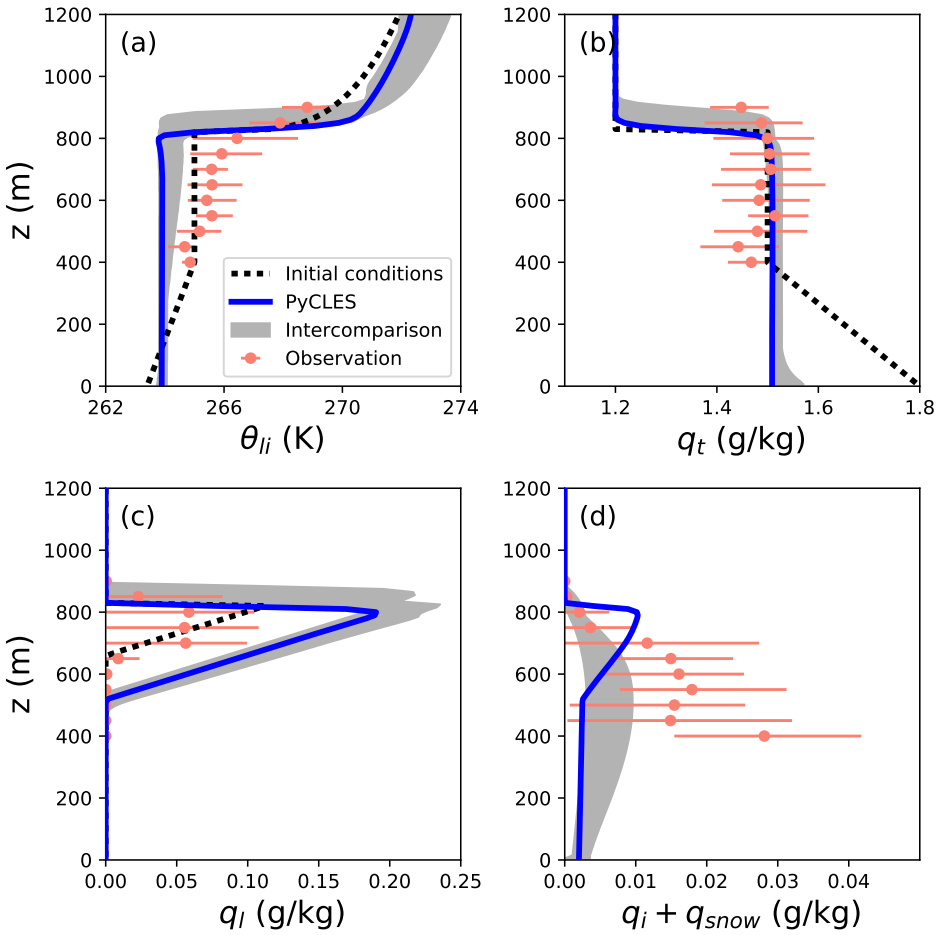

Figure 2. Domain mean profiles of (a) liquid ice potential temperature, (b) total water specific humidity, (c) cloud liquid water specific humidity, and (d) the sum of cloud ice and snow water specific humidity. Black dotted lines are the initial condition profiles. Gray shading shows the LES intercomparison range in *Ovchinnikov et al.* [2014]. The pink dots show the aircraft observations of flight 31 of ISDAC campaign on April 27, 2008. The horizontal lines indicate the 15–85 percentile range for the measurements binned every 50 m.

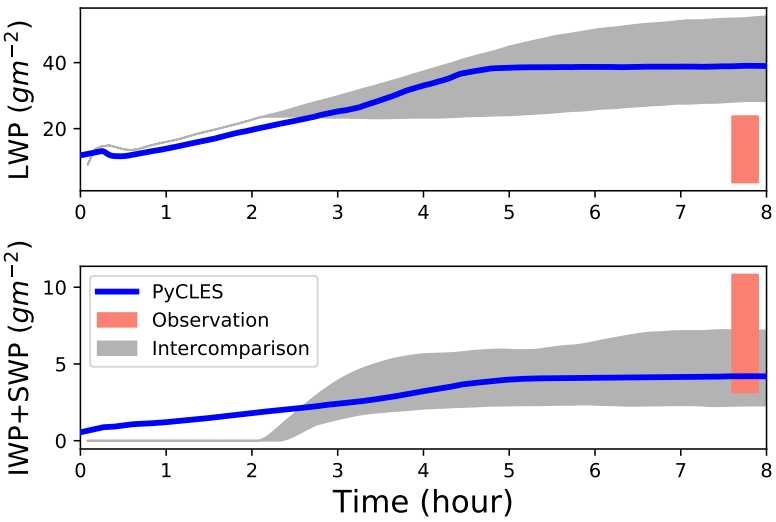

Figure 3. Timeseries of (top) liquid water path and (bottom) the sum of cloud ice and snow water path. Gray shading shows the LES intercomparison range in *Ovchinnikov et al.* [2014]. The pink bars show the range of observed values estimated using ISDAC flight 31 data in Figure 2.

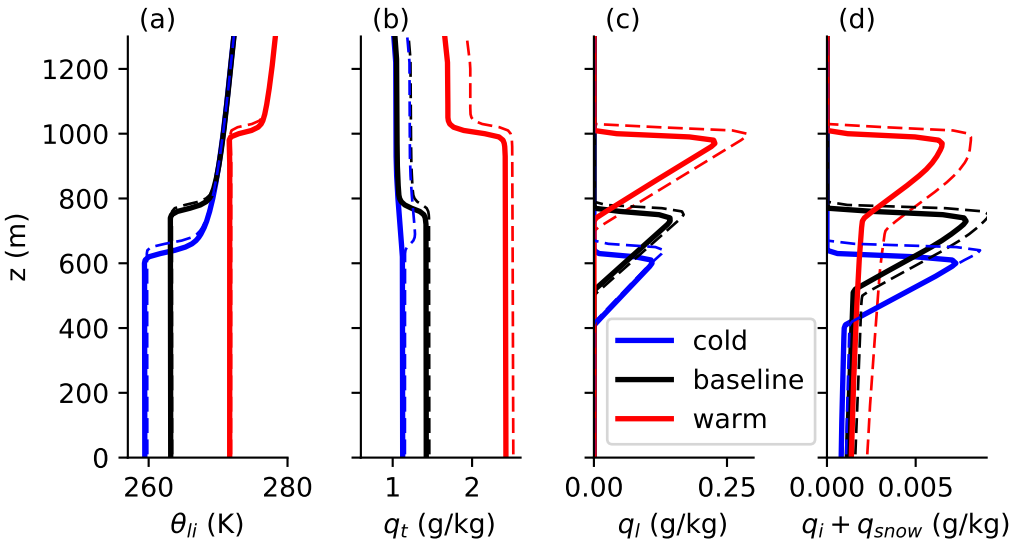

Figure 4. ISDAC-i domain mean profiles of (a) liquid ice potential temperature, (b) total water specific humidity, (c) liquid water specific humidity, and (d) the sum of cloud ice and snow water specific humidity. Solid lines are from simulations with RH=60%, and the dashed lines are with RH=70%.

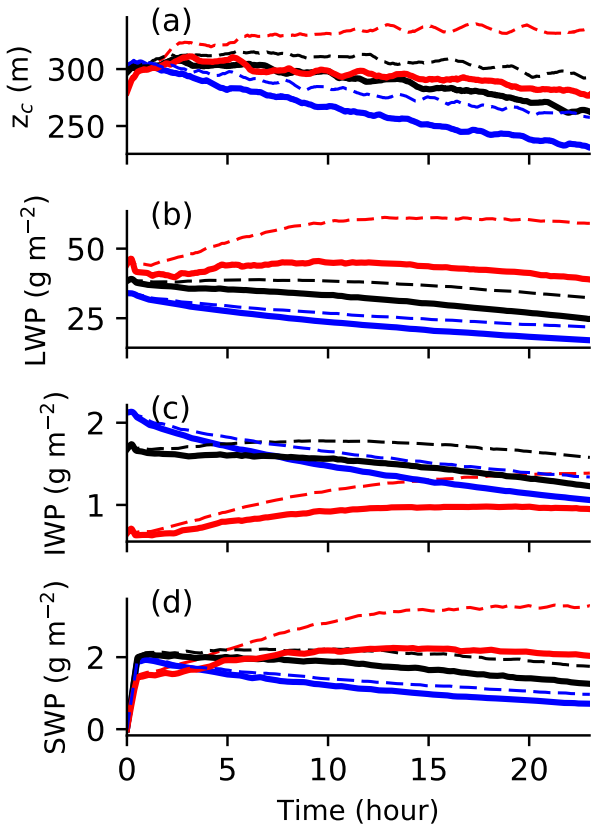

568 **Figure 5.** ISDAC-i timeseries of (a) cloud thickness, (b) liquid water path, (c) near-surface snow flux.
569 Colors are the same as in Figure 4. Data are smoothed over 1 hour periods for better visualization.

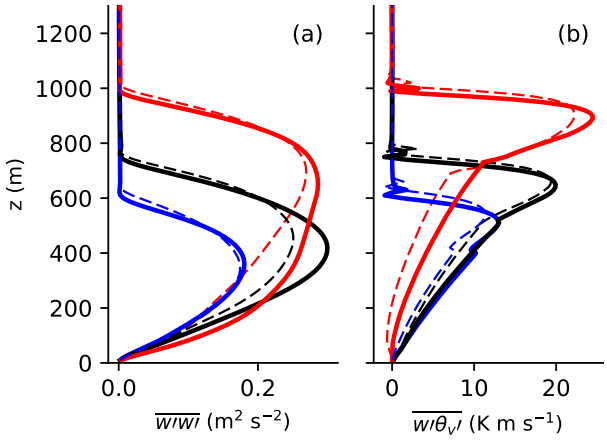

570 **Figure 6.** ISDAC-i domain mean profiles of (a) vertical velocity variance, and (b) vertical flux of virtual
571 potential temperature, representing buoyancy production of TKE. Colors are the same as in Figure 4. Solid
572 lines are from simulations with RH=60%, and the dashed lines are with RH=70%.

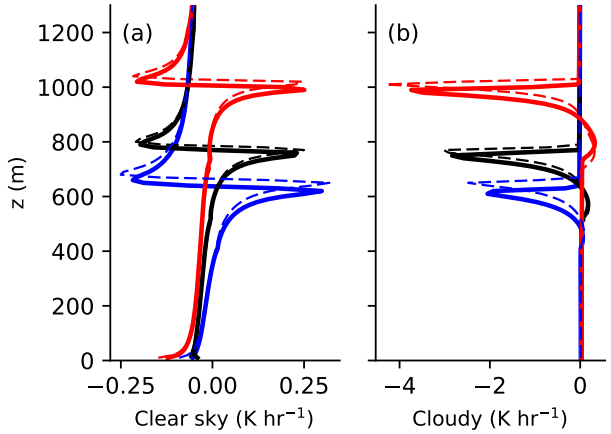

Figure 7. ISDAC-i domain mean profiles of (a) clear sky radiative heating rate, and (b) radiative heating rate due to cloud. Colors are the same as in Figure 4. Solid lines are from simulations with RH=60%, and the dashed lines are with RH=70%.

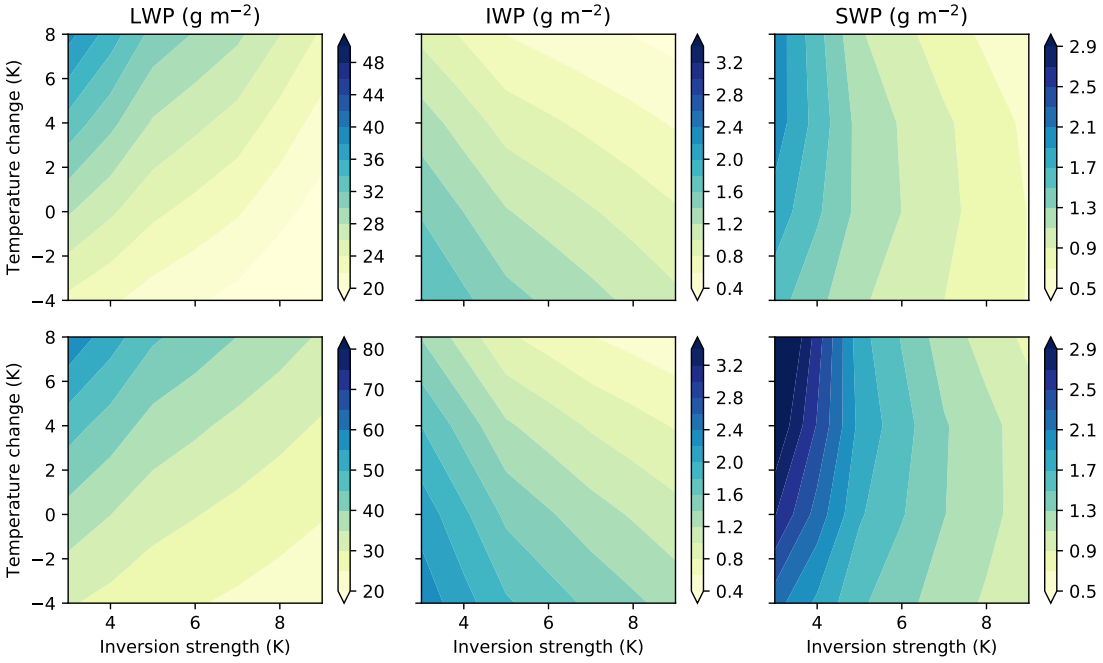

Figure 8. Liquid water path (LWP), ice water path (IWP), and snow water path (SWP) in LES ISDAC-i simulations averaged over the 24th hour. The horizontal axis shows the inversion strength, and the vertical axis shows uniform temperature change. Top panels show simulations with $\mathcal{H}_f = 60\%$, and bottom panels show simulations with $\mathcal{H}_f = 70\%$.

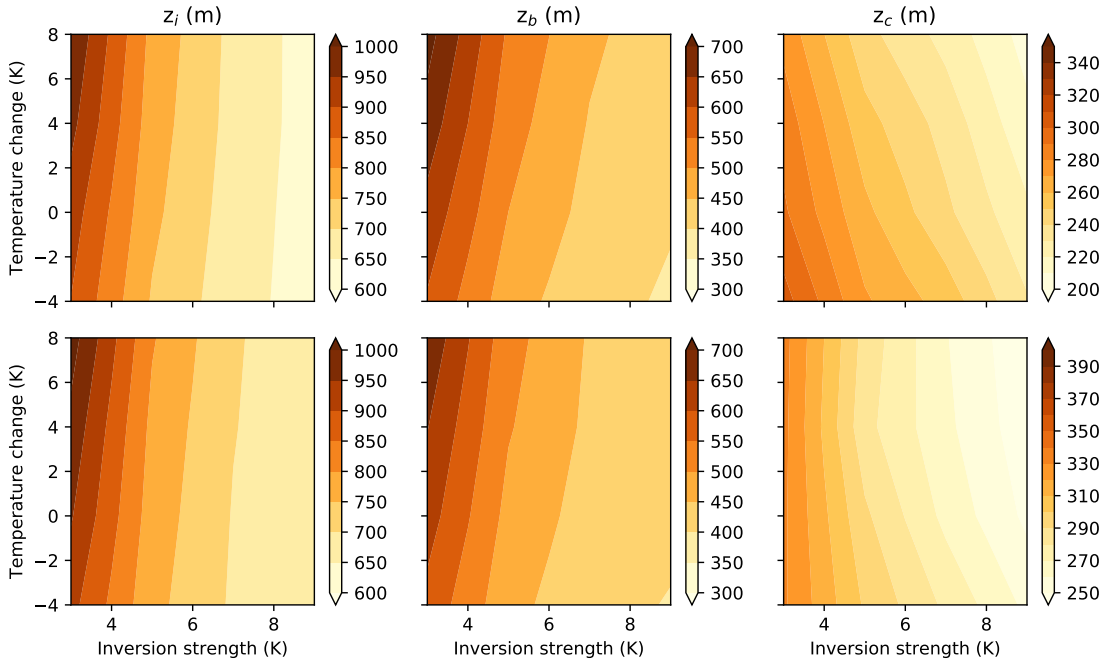

Figure 9. Same as Figure 8, but for LES cloud top height, cloud base height, and cloud thickness.

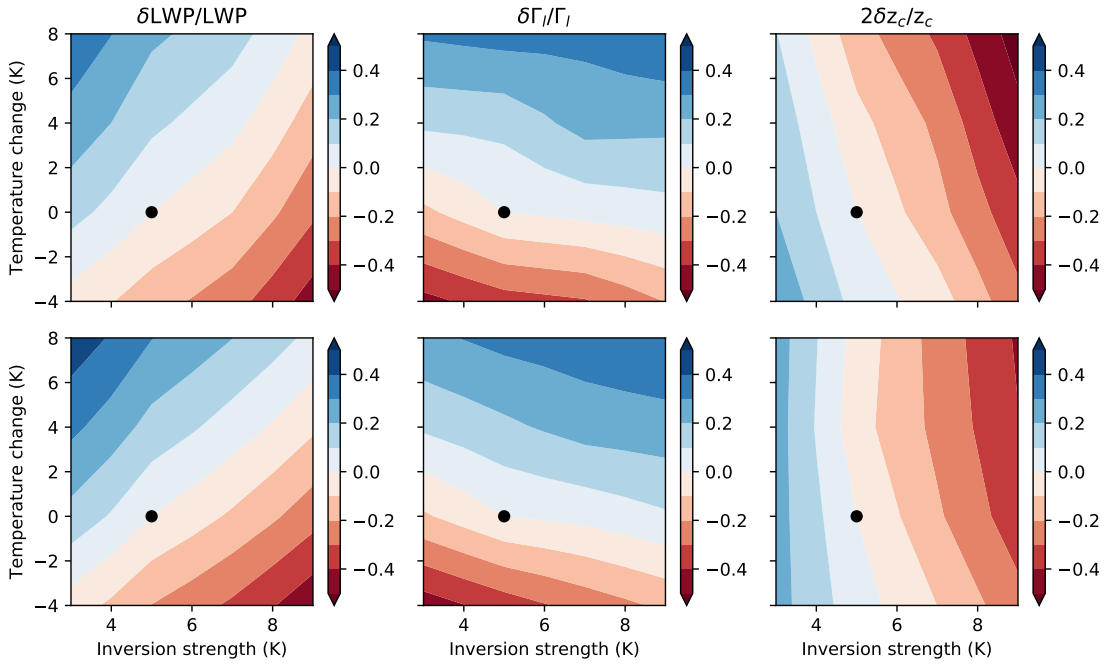

Figure 10. Same as Figure 8, but for LES estimated fractional LWP sensitivity, sensitivity due to fractional liquid lapse rate changes, and sensitivity due to fractional cloud thickness changes. All sensitivities are referenced to the *baseline* simulation indicated by the black dots. (9) for definition of the terms in the text.

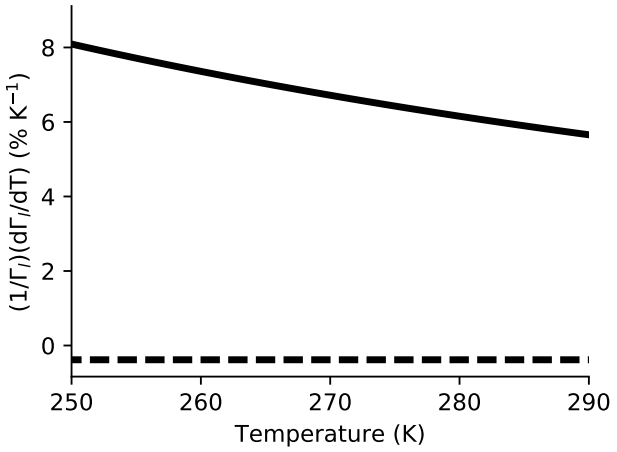

584 **Figure 11.** Fractional change of liquid water lapse rate with respect to temperature at 900 hPa. The solid
585 line shows the change due to temperature, and the dashed line shows the change due to pressure.

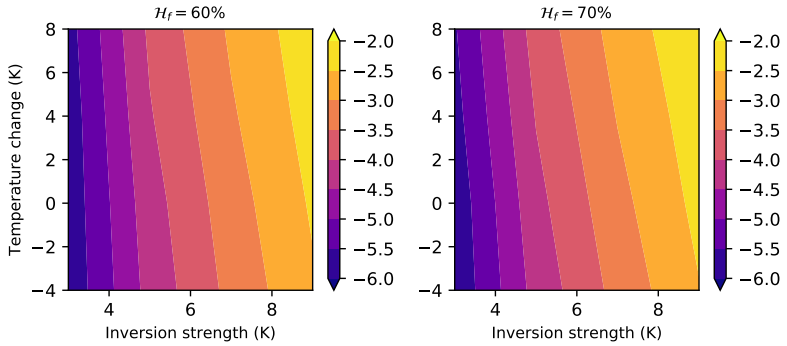

586 **Figure 12.** TOA longwave cloud radiative effect for LES simulations with (left) $\mathcal{H}_f = 60\%$ and (right)
587 $\mathcal{H}_f = 70\%$.

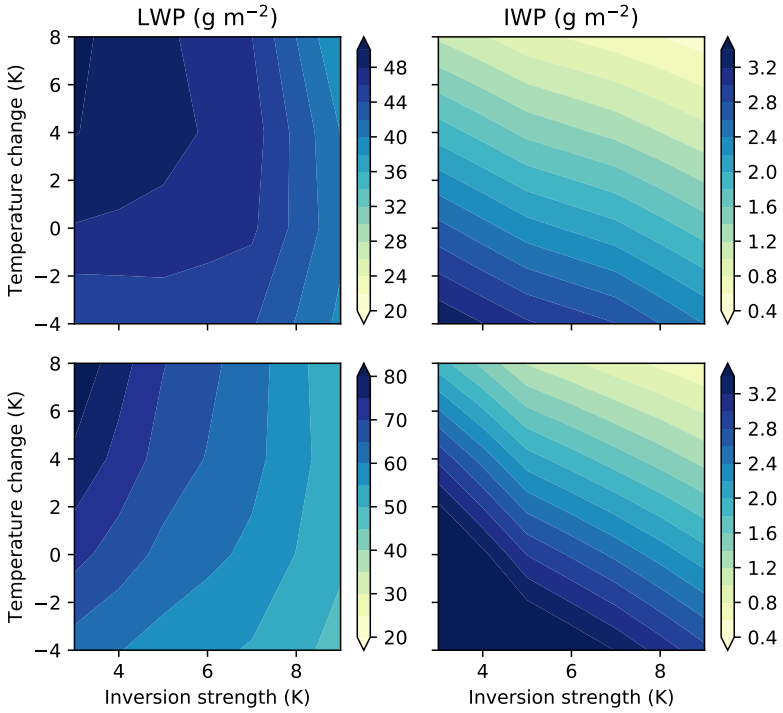

588 **Figure 13.** LWP and IWP in MLM ISDAC-i simulations averaged over the 24th hour. The horizontal axis
589 shows the inversion strength, and the vertical axis shows uniform temperature changes. Top panels show
590 simulations with $\mathcal{H}_f = 60\%$, and bottom panels show simulations with $\mathcal{H}_f = 70\%$.

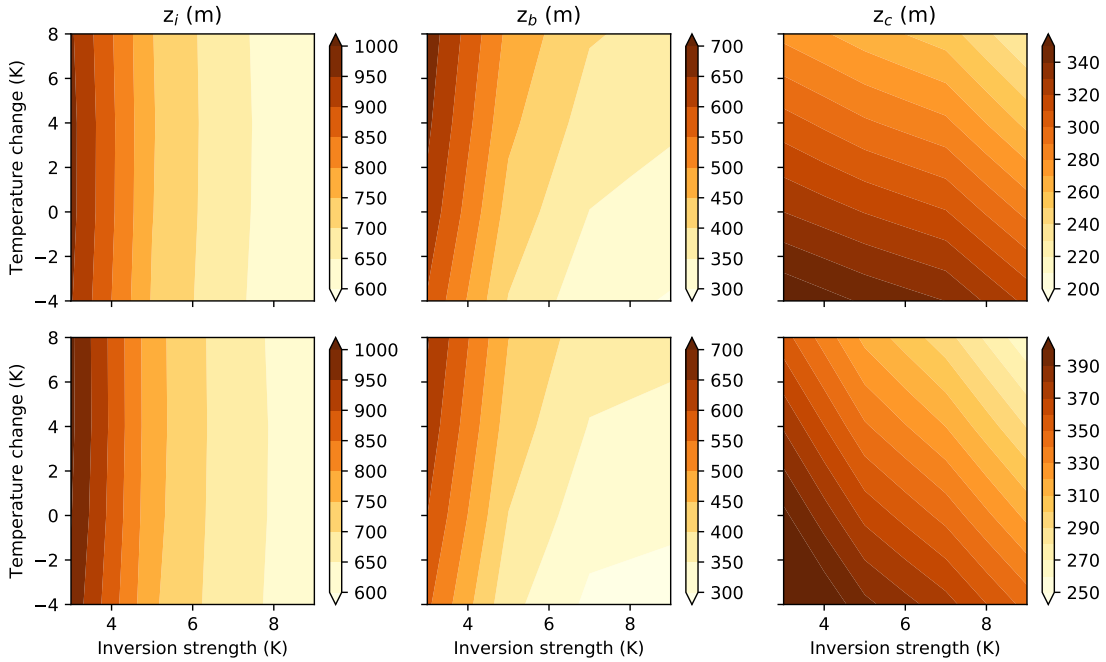

591 **Figure 14.** Same as Figure 13, but for MLM cloud top height, cloud base height, and cloud thickness.

A: MLM entrainment parameterization

Cloud-top entrainment rates w_e are diagnosed for all ISDAC-i LES simulations, using the mass balance equation (2). To parameterize w_e for MLM, we also diagnose $\Delta_i F_R$ and $\Delta\theta_{li}$ from the LES to get the linear-fit slope and intercept. The results are shown in Figure A.1. Overall, we obtain a good fit for ISDAC-i simulations using (5). Nearly 90% of the entrainment comes from the direct contribution of cloud-top radiative cooling.

B: List of Symbols

Unless otherwise noted, subscripts 0 indicate near-surface values, superscripts + indicate values right above the BL top.

Notation

$\boldsymbol{\Gamma_\theta}$ Potential temperature
$\boldsymbol{\Gamma_d}$ Dry adiabatic lapse rate
$\boldsymbol{\Gamma_l}$ Liquid water lapse rate
$\boldsymbol{\Gamma_m}$ Moist adiabatic lapse ratelapse rate in the free troposphere
$\boldsymbol{\Delta}$ Contrast across entire BL
$\boldsymbol{\Delta_i}$ Contrast across entrainment zone
$\boldsymbol{\theta_{li}}$ Potential temperature
$\boldsymbol{\theta_v}$ Virtual potential temperature
$\boldsymbol{\kappa}$ Thermal conductivity of air(?)
$\boldsymbol{\rho_a}$ Density of air
$\boldsymbol{\rho_i}$ Density of cloud ice
$\boldsymbol{\rho_l}$ Density of cloud liquid
$\boldsymbol{a}$ Entrainment coefficient
$\boldsymbol{c_p}$ Specific heat of air at constant pressure
$\boldsymbol{D}$ Water vapor diffusivity
$\boldsymbol{F_R}$ Longwave radiative flux
$\boldsymbol{\mathcal{H}_f}$ Relative humidity in the free troposphere
$\boldsymbol{L}$ Effective latent heat
$\boldsymbol{L_v}$ Latent heat of vaporization
$\boldsymbol{n}$ Exponent in liquid fraction
$\boldsymbol{q_i}$ Cloud ice water specific humidity
$\boldsymbol{q_l}$ Cloud liquid water specific humidity
$\boldsymbol{q_s}$ Saturation specific humidity
$\boldsymbol{q_{\mathrm{snow}}}$ Snow water specific humidity
$\boldsymbol{q_t}$ Total water specific humidity
$\boldsymbol{R_v}$ Gas constant for water vapor
$\boldsymbol{T}$ Temperature
$\boldsymbol{T_f}$ Freezing temperature of water
$\boldsymbol{T_i}$ Homogeneous nucleation temperature
$\boldsymbol{T_{\mathrm{LCL}}}$ Temperature at lifting condensation level
$\boldsymbol{w_e}$ Entrainment rate
$\boldsymbol{z_b}$ Cloud base height
$\boldsymbol{z_c}$ Cloud thickness
$\boldsymbol{z_i}$ Cloud top/BL height

Acknowledgments

The initial phases of this work were supported by the U.S. National Science Foundation Grants CCF 1048575. We thank Mikhail Ovchinnikov for providing the ISDAC LES intercomparison results, and Greg McFarquhar for his guidance on observational data. The ISDAC aircraft data were obtained from the Atmospheric Radiation Measurement (ARM) program archive, sponsored by the United States Department of Energy (DOE), Office of Science, Biological and Environmental Research (BER), Environmental Sciences Devision. We thank the two anonymous reviewers for their constructive comments. The PyCLES code is freely available at www.climate-dynamics.org. LES and MLM data are available from the corresponding author upon request.

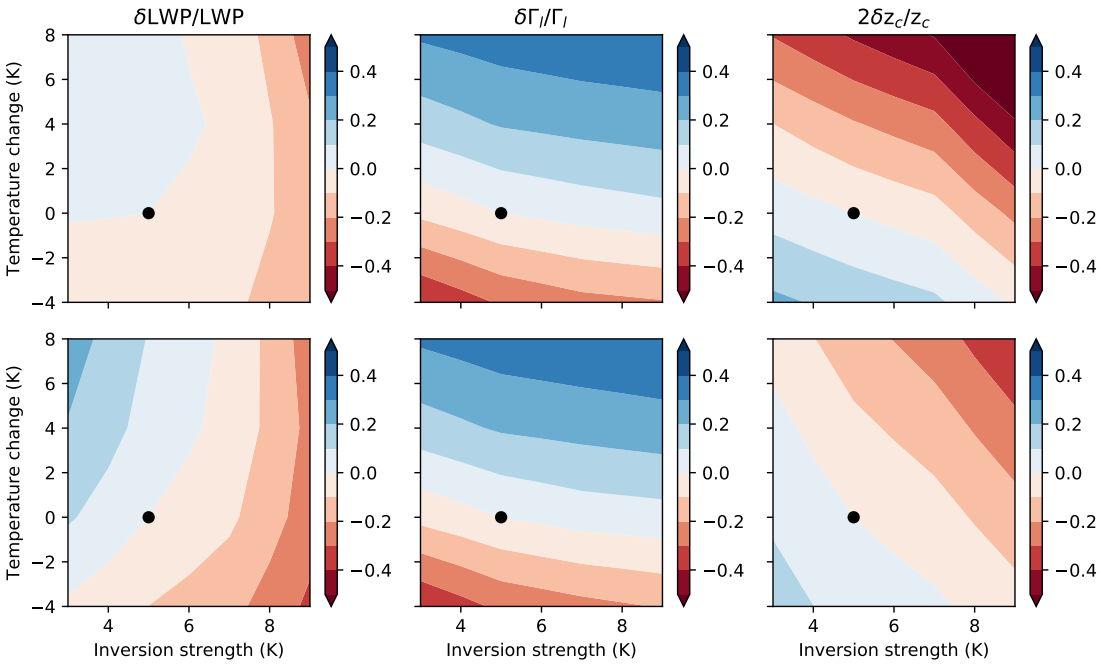

Figure 15. Same as Figure 13, but for MLM fractional LWP sensitivity, sensitivity due to fractional liquid lapse rate changes, and sensitivity due to fractional cloud thickness changes. All sensitivities are referenced to the *baseline* simulation indicated by the black dots.

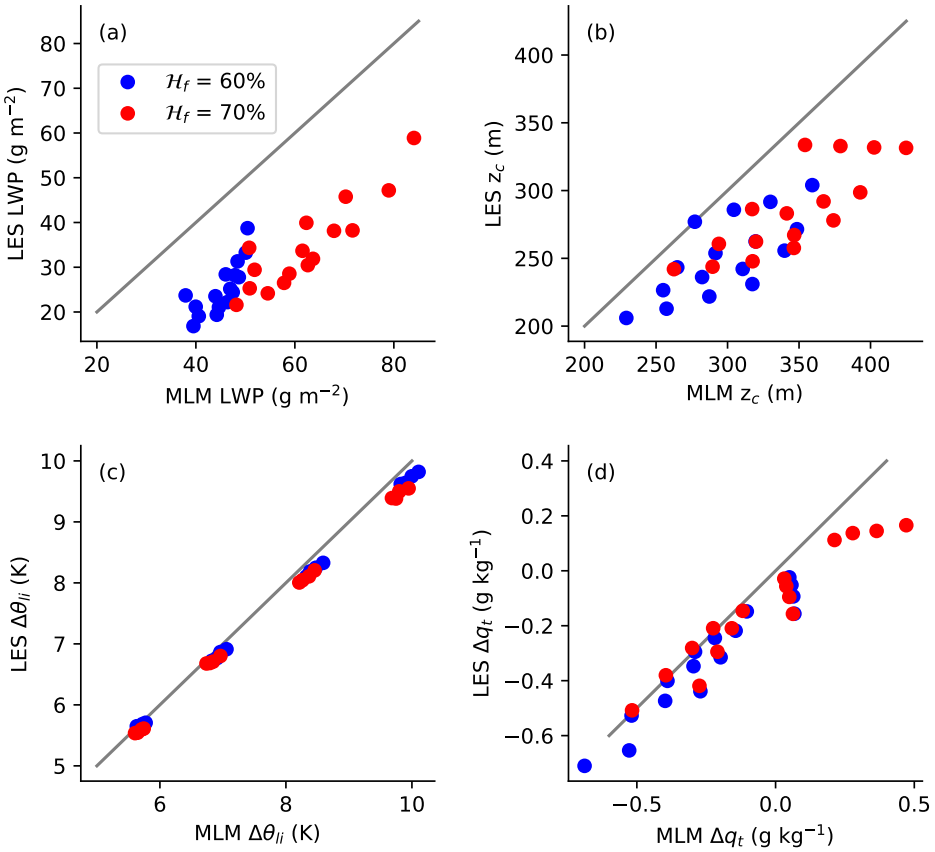

595 **Figure 16.** Scatter plots of (a) LWP, (b) cloud thickness z_c, (c) inversion strength $\Delta\theta_{li}$, and (d) specific
596 humidity jump q_t, from ISDAC-i simulations averaged at the last hour from MLM (x-axis) and LES (y-axis).
597 The gray lines indicate the 1:1 slope.

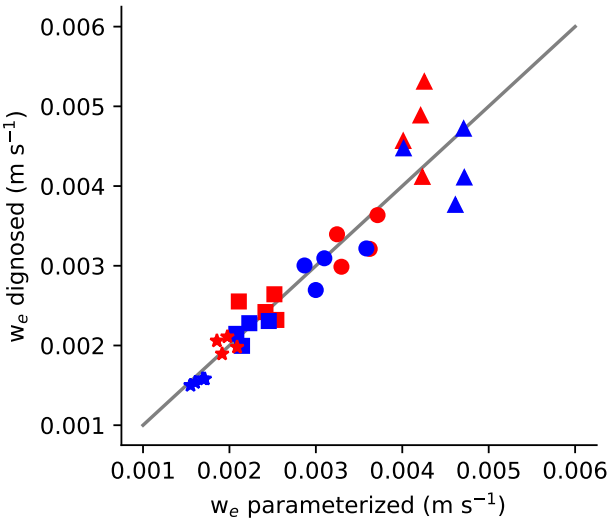

Figure A.1. Entrainment rates diagnosed from ISDAC-i LES simulations using Eq. (2), and parameterized using Eq. (5). The slope coefficient a = 0.85 and the intercept w_0 = 0.0004 m s^{-1} are from a linear fit, with r^2 = 0.89. Blue markers show simulations with $\mathcal{H}_f = 60\%$, and red with $\mathcal{H}_f = 70\%$. Marker types distinguish inversion strengths: 3 K (triangles), 5 K (circles), 7 K (squares), 9 K (stars).

References

Blossey, P. N., C. S. Bretherton, M. Zhang, A. Cheng, S. Endo, T. Heus, Y. Liu, A. P. Lock, S. R. de Roode, and K.-M. Xu (2013), Marine low cloud sensitivity to an idealized climate change: The CGILS LES intercomparison, *Journal of Advances in Modeling Earth Systems*, *5*(2), 234–258, doi:10.1002/jame.20025.

Boudala, F. S., G. A. Isaac, Q. Fu, and S. G. Cober (2002), Parameterization of effective ice particle size for high-latitude clouds, *International Journal of Climatology*, *22*(10), 1267–1284, doi:10.1002/joc.774.

Bretherton, C. S., and M. C. Wyant (1997), Moisture transport, lower-tropospheric stability, and decoupling of cloud-topped boundary layers, *Journal of the Atmospheric Sciences*, *54*(1), 148–167, doi:10.1175/1520-0469(1997)054<0148:MTLTSA>2.0.CO;2.

Cohen, J., J. A. Screen, J. C. Furtado, M. Barlow, D. Whittleston, D. Coumou, J. Francis, K. Dethloff, D. Entekhabi, J. Overland, et al. (2014), Recent Arctic amplification and extreme mid-latitude weather, *Nature Geoscience*, *7*(9), 627–637, doi: doi:10.1038/ngeo2234.

Cox, C. J., T. Uttal, C. N. Long, M. D. Shupe, R. S. Stone, and S. Starkweather (2016), The role of springtime Arctic clouds in determining autumn sea ice extent, *Journal of Climate*, *29*(18), 6581–6596, doi:10.1175/JCLI-D-16-0136.1.

Curry, J. A., J. L. Schramm, W. B. Rossow, and D. Randall (1996), Overview of Arctic cloud and radiation characteristics, *Journal of Climate*, *9*(8), 1731–1764, doi: 10.1175/1520-0442(1996)009<1731:OOACAR>2.0.CO;2.

Dal Gesso, S., A. P. Siebesma, S. R. de Roode, and J. M. van Wessem (2014), A mixed-layer model perspective on stratocumulus steady states in a perturbed climate, *Quarterly Journal of the Royal Meteorological Society*, *140*(684), 2119–2131, doi:10.1002/qj.2282.

de Boer, G., E. W. Eloranta, and M. D. Shupe (2009), Arctic mixed-phase stratiform cloud properties from multiple years of surface-based measurements at two high-latitude locations, *Journal of the Atmospheric Sciences*, *66*(9), 2874–2887, doi: 10.1175/2009JAS3029.1.

De Roode, S. R., A. P. Siebesma, S. D. Gesso, H. J. J. Jonker, J. Schalkwijk, and J. Sival (2014), A mixed-layer model study of the stratocumulus response to changes in large-scale conditions, *Journal of Advances in Modeling Earth Systems*, *6*(4), 1256–1270, doi:10.1002/2014MS000347.

Deardorff, J. W. (1980), Cloud top entrainment instability, *Journal of the Atmospheric Sciences*, *37*(1), 131–147, doi:10.1175/1520-0469(1980)037¡0131:CTEI¿2.0.CO;2.

Fan, J., S. Ghan, M. Ovchinnikov, X. Liu, P. J. Rasch, and A. Korolev (2011), Representation of arctic mixed-phase clouds and the Wegener-Bergeron-Findeisen process in climate models: Perspectives from a cloud-resolving study, *Journal of Geophysical Research: Atmospheres*, *116*(D1), doi:10.1029/2010JD015375, d00T07.

Fridlind, A. M., and A. S. Ackerman (2018), Chapter 7 - simulations of Arctic mixed-phase boundary layer clouds: Advances in understanding and outstanding questions, in *Mixed-Phase Clouds*, edited by C. Andronache, pp. 153 – 183, Elsevier, doi: 10.1016/B978-0-12-810549-8.00007-6.

Grabowski, W. W. (1998), Toward cloud resolving modeling of large-scale tropical circulations: A simple cloud microphysics parameterization, *Journal of the Atmospheric Sciences*, *55*(21), 3283–3298, doi:10.1175/1520-0469(1998)055<3283:TCRMOL>2.0.CO;2.

Graversen, R. G., and M. Wang (2009), Polar amplification in a coupled climate model with locked albedo, *Climate Dynamics*, *33*(5), 629–643, doi:10.1007/s00382-009-0535-6.

Holland, M. M., and C. M. Bitz (2003), Polar amplification of climate change in coupled models, *Climate Dynamics*, *21*(3), 221–232, doi:10.1007/s00382-003-0332-6.

Iacono, M. J., J. S. Delamere, E. J. Mlawer, M. W. Shephard, S. A. Clough, and W. D. Collins (2008), Radiative forcing by long-lived greenhouse gases: Calculations with

the AER radiative transfer models, *Journal of Geophysical Research: Atmospheres*, *113*(D13), doi:10.1029/2008JD009944, d13103.

Intrieri, J. M., M. D. Shupe, T. Uttal, and B. J. McCarty (2002), An annual cycle of Arctic cloud characteristics observed by radar and lidar at SHEBA, *Journal of Geophysical Research: Oceans*, *107*(C10), SHE 5–1–SHE 5–15, doi:10.1029/2000JC000423.

Karlsson, J., and G. Svensson (2013), Consequences of poor representation of Arctic sea-ice albedo and cloud-radiation interactions in the CMIP5 model ensemble, *Geophysical Research Letters*, *40*(16), 4374–4379, doi:10.1002/grl.50768.

Kaul, C. M., J. Teixeira, and K. Suzuki (2015), Sensitivities in large-eddy simulations of mixed-phase Arctic stratocumulus clouds using a simple microphysics approach, *Monthly Weather Review*, *143*(11), 4393–4421, doi:10.1175/MWR-D-14-00319.1.

Kay, J. E., and T. L'Ecuyer (2013), Observational constraints on Arctic ocean clouds and radiative fluxes during the early 21st century, *Journal of Geophysical Research: Atmospheres*, *118*(13), 7219–7236, doi:10.1002/jgrd.50489.

Kay, J. E., T. L'Ecuyer, H. Chepfer, N. Loeb, A. Morrison, and G. Cesana (2016), Recent advances in Arctic cloud and climate research, *Current Climate Change Reports*, *2*(4), 159–169, doi:10.1007/s40641-016-0051-9.

Klein, S. A., and D. L. Hartmann (1993), The seasonal cycle of low stratiform clouds, *Journal of Climate*, *6*(8), 1587–1606, doi:10.1175/1520-0442(1993)006<1587:TSCOLS>2.0.CO;2.

Lilly, D. K. (1968), Models of cloud-topped mixed layers under a strong inversion, *Quarterly Journal of the Royal Meteorological Society*, *94*(401), 292–309, doi:10.1002/qj.49709440106.

Manabe, S., and R. T. Wetherald (1975), The effects of doubling the CO_2 concentration on the climate of a general circulation model, *Journal of the Atmospheric Sciences*, *32*(1), 3–15, doi:10.1175/1520-0469(1975)032<0003:TEODTC>2.0.CO;2.

Martin, G. M., D. W. Johnson, and A. Spice (1994), The measurement and parameterization of effective radius of droplets in warm stratocumulus clouds, *Journal of the Atmospheric Sciences*, *51*(13), 1823–1842, doi:10.1175/1520-0469(1994)051<1823:TMAPOE>2.0.CO;2.

McFarquhar, G. M., S. Ghan, J. Verlinde, A. Korolev, J. W. Strapp, B. Schmid, J. M. Tomlinson, M. Wolde, S. D. Brooks, D. Cziczo, M. K. Dubey, J. Fan, C. Flynn, I. Gultepe, J. Hubbe, M. K. Gilles, A. Laskin, P. Lawson, W. R. Leaitch, P. Liu, X. Liu, D. Lubin, C. Mazzoleni, A.-M. Macdonald, R. C. Moffet, H. Morrison, M. Ovchinnikov, M. D. Shupe, D. D. Turner, S. Xie, A. Zelenyuk, K. Bae, M. Freer, and A. Glen (2011), Indirect and Semi-direct Aerosol Campaign, *Bulletin of the American Meteorological Society*, *92*(2), 183–201, doi:10.1175/2010BAMS2935.1.

Mellado, J. P. (2017), Cloud-top entrainment in stratocumulus clouds, *Annual Review of Fluid Mechanics*, *49*(1), 145–169, doi:10.1146/annurev-fluid-010816-060231.

Moeng, C.-H. (2000), Entrainment rate, cloud fraction, and liquid water path of PBL stratocumulus clouds, *Journal of the Atmospheric Sciences*, *57*(21), 3627–3643, doi:10.1175/1520-0469(2000)057<3627:ERCFAL>2.0.CO;2.

Moeng, C.-H., P. P. Sullivan, and B. Stevens (1999), Including radiative effects in an entrainment rate formula for buoyancy-driven PBLs, *Journal of the Atmospheric Sciences*, *56*(8), 1031–1049, doi:10.1175/1520-0469(1999)056<1031:IREIAE>2.0.CO;2.

Morrison, H., P. Zuidema, G. M. McFarquhar, A. Bansemer, and A. J. Heymsfield (2011), Snow microphysical observations in shallow mixed-phase and deep frontal Arctic cloud systems, *Quarterly Journal of the Royal Meteorological Society*, *137*(659), 1589–1601, doi:10.1002/qj.840.

Ovchinnikov, M., A. S. Ackerman, A. Avramov, A. Cheng, J. Fan, A. M. Fridlind, S. Ghan, J. Harrington, C. Hoose, A. Korolev, G. M. McFarquhar, H. Morrison, M. Paukert, J. Savre, B. J. Shipway, M. D. Shupe, A. Solomon, and K. Sulia (2014), Intercomparison of large-eddy simulations of Arctic mixed-phase clouds: Importance of ice size distribution assumptions, *Journal of Advances in Modeling Earth Systems*, *6*(1),

223–248, doi:10.1002/2013MS000282.

Pithan, F., and T. Mauritsen (2014), Arctic amplification dominated by temperature feedbacks in contemporary climate models, *Nature Geoscience*, *7*(3), 181–184, doi:10.1038/ngeo2071.

Pressel, K. G., C. M. Kaul, T. Schneider, Z. Tan, and S. Mishra (2015), Large-eddy simulation in an anelastic framework with closed water and entropy balances, *Journal of Advances in Modeling Earth Systems*, doi:10.1002/2015MS000496.

Pressel, K. G., S. Mishra, T. Schneider, C. M. Kaul, and Z. Tan (2017), Numerics and subgrid-scale modeling in large eddy simulations of stratocumulus clouds, *Journal of Advances in Modeling Earth Systems*, doi:10.1002/2016MS000778.

Savre, J., A. M. L. Ekman, and G. Svensson (2014), Technical note: Introduction to MIMICA, a large-eddy simulation solver for cloudy planetary boundary layers, *Journal of Advances in Modeling Earth Systems*, *6*(3), 630–649, doi:10.1002/2013MS000292.

Savre, J., A. M. L. Ekman, G. Svensson, and M. Tjernstrm (2015), Large-eddy simulations of an Arctic mixed-phase stratiform cloud observed during ISDAC: sensitivity to moisture aloft, surface fluxes and large-scale forcing, *Quarterly Journal of the Royal Meteorological Society*, *141*(689), 1177–1190, doi:10.1002/qj.2425.

Schneider, T., and I. M. Held (2001), Discriminants of twentieth-century changes in Earth surface temperatures, *Journal of Climate*, *14*(3), 249–254, doi:10.1175/1520-0442(2001)014¡0249:LDOTCC¿2.0.CO;2.

Screen, J. A., C. Deser, and I. Simmonds (2012), Local and remote controls on observed Arctic warming, *Geophysical Research Letters*, *39*(10), doi:10.1029/2012GL051598, L10709.

Sedlar, J., and M. Tjernström (2009), Stratiform cloud—inversion characterization during the Arctic melt season, *Boundary-Layer Meteorology*, *132*(3), 455–474, doi:10.1007/s10546-009-9407-1.

Serreze, M. C., A. P. Barrett, J. C. Stroeve, D. N. Kindig, and M. M. Holland (2009), The emergence of surface-based Arctic amplification, *The Cryosphere*, *3*(1), 11–19, doi:10.5194/tc-3-11-2009.

Serreze, M. C., A. P. Barrett, and J. Stroeve (2012), Recent changes in tropospheric water vapor over the Arctic as assessed from radiosondes and atmospheric reanalyses, *Journal of Geophysical Research: Atmospheres*, *117*(D10), doi:10.1029/2011JD017421, d10104.

Sherwood, S. C., W. Ingram, Y. Tsushima, M. Satoh, M. Roberts, P. L. Vidale, and P. A. O'Gorman (2010), Relative humidity changes in a warmer climate, *Journal of Geophysical Research: Atmospheres*, *115*(D9), doi:10.1029/2009JD012585, d09104.

Solomon, A., M. D. Shupe, O. Persson, H. Morrison, T. Yamaguchi, P. M. Caldwell, and G. de Boer (2014), The sensitivity of springtime Arctic mixed-phase stratocumulus clouds to surface-layer and cloud-top inversion-layer moisture sources, *Journal of the Atmospheric Sciences*, *71*(2), 574–595, doi:10.1175/JAS-D-13-0179.1.

Stevens, B. (2006), Bulk boundary-layer concepts for simplified models of tropical dynamics, *Theor. Comput. Fluid Dyn.*, *20*, 279–304, doi:0.1007/s00162-006-0032-z.

Straka, J. M. (2009), *Cloud and Precipitation Microphysics: Principles and Parameterizations*, Cambridge University Press, doi:10.1017/CBO9780511581168.

Stroeve, J. C., M. C. Serreze, M. M. Holland, J. E. Kay, J. Malanik, and A. P. Barrett (2012), The Arctic's rapidly shrinking sea ice cover: a research synthesis, *Climatic Change*, *110*(3), 1005–1027, doi:10.1007/s10584-011-0101-1.

Stull, R. B. (1988), Boundary Layer Clouds, in *An Introduction to Boundary Layer Meteorology*, edited by R. B. Stull, pp. 545–585, Springer Netherlands, Dordrecht, dOI:10.1007/978-94-009-3027-8_13.

Tan, Z., T. Schneider, J. Teixeira, and K. G. Pressel (2016), Large-eddy simulation of subtropical cloud-topped boundary layers: 1. A forcing framework with closed surface energy balance, *Journal of Advances in Modeling Earth Systems*, doi:10.1002/2016MS000655.

Tan, Z., T. Schneider, J. Teixeira, and K. G. Pressel (2017), Large-eddy simulation of subtropical cloud-topped boundary layers: 2. Cloud response to climate change, *Journal of Advances in Modeling Earth Systems*, doi:10.1002/2016MS000804.

Tjernström, M., and R. G. Graversen (2009), The vertical structure of the lower Arctic troposphere analysed from observations and the ERA-40 reanalysis, *Quarterly Journal of the Royal Meteorological Society*, *135*(639), 431–443, doi:10.1002/qj.380.

Tripoli, G. J., and W. R. Cotton (1981), The use of ice-liquid water potential temperature as a thermodynamic variable in deep atmospheric models, *Monthly Weather Review*, *109*(5), 1094–1102, doi:10.1175/1520-0493(1981)109<1094:TUOLLW>2.0.CO;2.

van der Dussen, J. J., S. R. de Roode, S. Dal Gesso, and A. P. Siebesma (2015), An LES model study of the influence of the free tropospheric thermodynamic conditions on the stratocumulus response to a climate perturbation, *Journal of Advances in Modeling Earth Systems*, *7*(2), 670–691, doi:10.1002/2014MS000380.

Vavrus, S., D. Waliser, A. Schweiger, and J. Francis (2009), Simulations of 20th and 21st century Arctic cloud amount in the global climate models assessed in the IPCC AR4, *Climate Dynamics*, *33*(7), 1099, doi:10.1007/s00382-008-0475-6.

Wang, X., and J. R. Key (2005), Arctic surface, cloud, and radiation properties based on the AVHRR Polar Pathfinder dataset. part II: Recent trends, *Journal of Climate*, *18*(14), 2575–2593, doi:10.1175/JCLI3439.1.

Wetherald, R. T., and S. Manabe (1975), The effects of changing the solar constant on the climate of a general circulation model, *J. Atmos. Sci.*, *32*, 2044–2059.

Wood, R. (2012), Stratocumulus clouds, *Monthly Weather Review*, *140*(8), 2373–2423, doi:10.1175/MWR-D-11-00121.1.